The Astrophysical Journal, 807:72 (12pp), 2015 July 1 doi:10.1088/0004-637X/807/1/72

IMAGING AND SPECTRAL OBSERVATIONS OF QUASI-PERIODIC PULSATIONS IN A SOLAR FLARE

D. Li[1,2], Z. J. Ning[1], and Q. M. Zhang[1]
[1] Key Laboratory of Dark Matter and Space Astronomy, Purple Mountain Observatory, CAS, Nanjing 210008, China; lidong@pmo.ac.cn.
[2] University of Chinese Academy of Sciences, Beijing 100049, China
Received 2015 March 9; accepted 2015 May 11; published 2015 July 1

ABSTRACT

We explore the quasi-periodic pulsations (QPPs) in a solar flare observed by *Fermi* Gamma-ray Burst Monitor, *Solar Dynamics Observatory*, *Solar Terrestrial Relations Observatory*, and *Interface Region Imaging Spectrograph* (*IRIS*) on 2014 September 10. QPPs are identified as the regular and periodic peaks on the rapidly varying components, which are the light curves after removing the slowly varying components. The QPPs display only three peaks at the beginning on the hard X-ray emissions, but 10 peaks on the chromospheric and coronal line emissions, and more than seven peaks (each peak corresponds to a type III burst on the dynamic spectra) at the radio emissions. A uniform quasi-period of about 4 minutes is detected among them. AIA imaging observations exhibit that the 4-minute QPPs originate from the flare ribbon and tend to appear on the ribbon front. *IRIS* spectral observations show that each peak of the QPPs tends to a broad line width and a red Doppler velocity at C I, O IV, Si IV, and Fe XXI lines. Our findings indicate that the QPPs are produced by the non-thermal electrons that are accelerated by the induced quasi-periodic magnetic reconnections in this flare.

Key words: line: profiles – Sun: oscillations – Sun: radio radiation – Sun: UV radiation – Sun: X-rays, gamma-rays – techniques: spectroscopic

Supporting material: animation

1. INTRODUCTION

Quasi-periodic pulsations (QPPs) are regular phenomena and common features observed in the solar flare emissions. In a typical event, QPP displays as the periodic peaks on the light curve. Each peak has a similar lifetime, which results in a regular interval among them. Therefore, the QPPs are characterized by the repetition or the periodicity. They are observed with the typical periods ranging from milliseconds (e.g., Karlický et al. 2005; Tan et al. 2010) through seconds (e.g., Hoyng et al. 1976; Lipa 1978; Bogovalov et al. 1983, 1984; Mangeney & Pick 1989; Zhao et al. 1991; Aschwanden et al. 1994b; Ning et al. 2005; Zimovets & Struminsky 2010; Nakariakov et al. 2010) to minutes (e.g., Nakariakov et al. 1999; Aschwanden et al. 2002; De Moortel et al. 2002; Foullon et al. 2005; Ofman & Sui 2006; Li & Gan 2008; Sych et al. 2009; Tan et al. 2010; Su et al. 2012a; Ning 2014). The previous observations show that their periods are positively correlated with the major radius of the flaring loop (Aschwanden et al. 1998). The short QPPs are thought to be associated with kinetic processes caused by the dynamic interaction of electromagnetic plasma or waves with energetic particles trapped in closed magnetic fields (Aschwanden 1987; Nakariakov & Melnikov 2009). The long QPPs are usually associated with active region dynamics and global oscillations of the Sun (Chen & Priest 2006; Nakariakov & Melnikov 2009).

The QPPs are detected in a broad wavelength range from radio (e.g., Mangeney & Pick 1989; Zhao et al. 1991; Aschwanden et al. 1994b; Kliem et al. 2000; Karlický et al. 2005; Ning et al. 2005; Tan et al. 2010) through visible and extreme-ultraviolet (EUV; e.g., Nakariakov et al. 1999; Aschwanden et al. 2002; De Moortel et al. 2002; Ofman & Wang 2002; Su et al. 2012a, 2012b) to X-rays (e.g., Hoyng et al. 1976; Lipa 1978; Bogovalov et al. 1983, 1984; Foullon et al. 2005; Ofman & Sui 2006; Nakariakov et al. 2006, 2010; Li & Gan 2008; Zimovets & Struminsky 2010; Ning 2014), and even to γ-rays (Nakariakov et al. 2010). In radio emissions, the QPPs are usually detected as the periodic type III bursts. Mangeney & Pick (1989) have reported that the periods range from 1 to 6 s. The statistical studies of the quasi-periodicity in the normal and reverse slope type III bursts have been reported by Aschwanden et al. (1994b) and Ning et al. (2005), respectively. Both of them obtained the mean period of ~2 s and believed that the periodicity is due to the periodic acceleration processes in the solar flares. At EUV wavelengths, QPPs are usually detected in coronal loops. Moreover, using the spectral observations, the QPPs in Doppler velocity and line width of the hot and cool lines are also detected (Kliem et al. 2002; Tian et al. 2011). For example, using the Solar Ultraviolet Measurement of Emitted Radiation spectrometer on board *Solar and Heliospheric Observatory*, the Doppler velocity in hot lines (>6 MK) is detected to exhibit QPPs with a period of about 10 minutes (Ofman & Wang 2002; Wang et al. 2002, 2003). With the Bragg Crystal Spectrometer on *Yohkoh*, the Doppler velocity in the flare emission lines (e.g., S XV and Ca XIX) is observed to display QPPs with a period of several minutes (Mariska 2005, 2006). Tian et al. (2011) found that the QPPs are correlated with line intensity, Doppler velocity, and line width from the observations of *Hinode* EUV Imaging Spectrometer. In the X-ray and γ-ray channels, the QPPs with a short period of a few seconds are detected by Hoyng et al. (1976) and Bogovalov et al. (1983). Using *RHESSI* observations, the 2005 January 19 solar flare displays QPPs with a period of 2–4 minutes at hard X-ray (HXR) emissions (Ofman & Sui 2006), while the 2002 December 26 solar flare exhibits 2-minute QPPs at the soft X-ray (SXR) emissions (Ning 2014). Some flares exhibit similar QPPs in a broad wavelength (e.g., Nakajima et al. 1983; Aschwanden et al. 1995; Asai et al. 2001). For example, the 1998 November 10 solar flare displays the QPPs with a period of 6 s in both radio and X-ray emissions (Asai

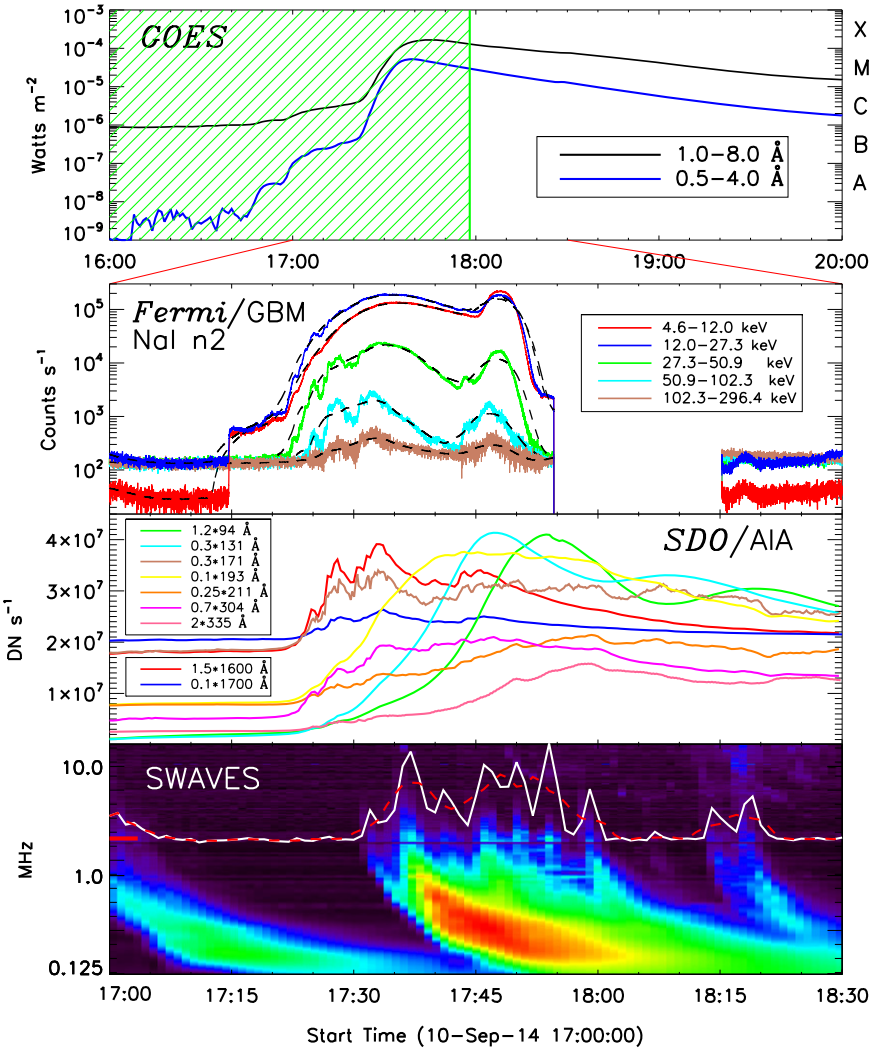

Figure 1. Top: *GOES* SXR flux from 16:00 UT to 20:00 UT on 2014 September 10. The vertical green line marks the end time of *IRIS* observations. Second: X-ray light curves from *Fermi*/GBM (detector n2) at five energy channels. The dashed lines represent the slowly varying components. Third: AIA light curves integrated from the flare region marked with the blue box in Figure 3. Bottom: radio dynamic spectra between 0.125 and 16.075 MHz from *STEREO*/WAVES. The white profile is the radio emission at frequency ~2.19 MHz, which is marked with the short red line, and the red dashed line represents the slowly varying components.

et al. 2001), while Nakajima et al. (1983) reported QPPs with a quasi-period of 8 s from radio, HXR, and γ-ray emissions.

The generation mechanism of QPPs is still an open issue in the documents (Aschwanden 1987; Nakariakov et al. 2006; Li & Gan 2008; Nakariakov & Melnikov 2009; Ning 2014). Basically, QPPs are thought to be related with waves or energetic particles (electrons). Actually, MHD waves, such as slow magnetoacoustic, fast kink, and sausage waves (Roberts et al. 1984; Nakariakov & Melnikov 2009), have been used to explain the generation of the QPPs in radio (Nakariakov et al. 2004; Kupriyanova et al. 2010; Tan et al. 2010), EUV (Ofman & Wang 2002; Mariska 2006; Tian et al. 2011; Su et al. 2012a, 2012b), and X-ray or γ-ray (Nakariakov et al. 2004; Foullon et al. 2005; Nakariakov et al. 2010; Zimovets & Struminsky 2010) emissions. On the other hand, the QPPs could be explained by the emissions from the non-thermal electrons that are accelerated by the quasi-periodic magnetic reconnection. And the quasi-periodic reconnection can be spontaneous (Kliem et al. 2000; Karlický 2004; Karlický et al. 2005; Murray et al. 2009) or may be modulated by MHD waves, i.e., the slow waves (Chen & Priest 2006; Nakariakov & Zimovets 2011; Li & Zhang 2015) or the fast waves (Nakariakov et al. 2006; Ofman & Sui 2006; Nakariakov & Melnikov 2009; Liu et al. 2011). Until now, QPPs are poorly observed in the same flare with imaging and spectral observations simultaneously, which could provide an opportunity to improve the QPPs' origination and physics model. In this paper, we analyze the QPPs in a solar flare on 2014 September 10 observed by *Fermi*, *Solar Dynamics Observatory* (*SDO*), *Solar Terrestrial Relations Observatory* (*STEREO*), and *Interface Region Imaging Spectrograph* (*IRIS*) at HXR, EUV, and radio wavelengths.

2. OBSERVATIONS AND DATA ANALYSIS

The solar flare studied in this paper takes place in NOAA AR 12158 (N11°, E05°) on 2014 September 10, and it is accompanied by a halo coronal mass ejection. It is an X1.6 flare, which starts at 17:21 UT and reaches its maximum at 17:45 UT from *GOES* SXR flux. Figure 1 shows the light curves detected by *GOES*, *Fermi*/Gamma-ray Burst Monitor (GBM), and *SDO*/AIA and the dynamic spectra detected by *STEREO*/WAVES (SWAVES). The top panel gives the *GOES*

observations at two SXR channels, such as 1.0–8.0 Å (black) and 0.5–4.0 Å (blue). The shaded interval marks *IRIS* observations. The second panel shows the *Fermi* light curves at five energy channels, such as 4.6–12.0, 12.0–27.3, 27.3–50.9, 50.9–102.3, and 102.3–296.4 keV. They are detected by the n2 detector, whose direction angle to the Sun is stable (~60°) during this flare, especially at the interval from 17:10 UT to 17:45 UT, while the other detectors change their direction angles frequently. After 17:45 UT, the n2 detector shifts its direction angle from ~60° to ~45° and then becomes bigger again, which results in an X-ray peak around 17:50 UT. Therefore, it is not the real X-ray emission peak. There is a data gap after 17:54 UT. The time resolution of *Fermi* is 0.256 s, but it becomes 0.064 s automatically in the flare state (Meegan et al. 2009). We interpolate all the data into an uniform resolution of 0.256 s in the second panel. Such a cadence is enough to analyze the QPPs with a period of several minutes in this paper. The third panel shows the *SDO*/AIA light curves (integration from images) at nine wavelengths: 1600, 1700, 94, 131, 171, 193, 211, 304, and 335 Å. Their time resolutions are 24 s here. The bottom panel displays the radio dynamic spectra between ~0.125 and ~16.075 MHz observed by SWAVES aboard *STEREO-B*. The time resolution is 1 minute (Rucker et al. 2005). There is a group of solar radio type III bursts.

Figure 1 shows that there are several peaks during the impulsive phase at HXR light curves, i.e., from 17:21 to 17:40 UT. These peaks seem to be regular and periodic, and they look like the QPPs. However, they are superposed by a gradual background emission. Meanwhile, there are several type III bursts on the dynamic spectra. The radio light curve at 2.19 MHz (white line) exhibits the regular peaks with a quasi-period. In order to distinguish these peaks from the background, we decompose each light curve at X-ray and radio bands into a slowly varying component and a rapidly varying component. The slowly varying component (the background emission) is the smoothing original data. Here the smoothing window is different for various data with similar cadences. For example, the smoothing window is 1000 points for *Fermi* data and 4 points for SWAVES data. The dashed lines overplotted on the original light curves in Figure 1 are their slowly varying components.

QPPs are identified from the rapidly varying components, which are the light curves subtracted by the slowly varying components. As shown in Figure 1, we get the slowly varying components at five X-ray bands (black dashed lines) and at one radio frequency (red dashed lines). Figure 2 gives the rapidly varying components at three HXR channels of 27.3–50.9 keV, 50.9–102.3 keV, and 102.3–296.4 keV and one radio frequency at ~2.19 MHz. These three HXR channels display the typical QPPs with three regular peaks, which are marked by the numbers "1," "2," and "3" between 17:24 UT and 17:36 UT. There are no similar peaks in the other two X-ray bands below 27 keV. However, there are seven regular peaks between 17:32 and 18:01 on the radio frequency at ~2.19 MHz, marked by the numbers. Then the wavelet analysis is used to detect the period of the QPPs. The bottom panels of Figure 2 show their wavelet power spectra, which confirm the QPPs' feature with a similar period of about 4 minutes at both HXR and radio emissions. As mentioned earlier, the HXR peaks at 17:50 UT are not real, although they are the emissions from the Sun.

There are two interesting facts to be mentioned here. First, the HXR light curves display the QPPs from 17:24 UT to 17:36 UT, while the radio emissions exhibit the QPPs from 17:32 UT to 18:01 UT. Namely, there is a delay of about 8 minutes between their onset. Second, the QPPs show three peaks at HXR channels, but more than seven peaks at radio frequency. Each peak is a type III burst on the dynamic spectra. The question is whether the QPPs at HXR are related to that at the radio in this event, and whether the QPPs at HXR and radio originate the same process during the flare. In order to answer these questions, imaging and spectral analyses of the QPPs are needed. High spatial and time resolution images of *SDO*/AIA and high spectral resolution of *IRIS* observations give us the opportunity to study the QPPs' origination in the 2014 September 10 flare.

Figure 3 shows the *SDO*/AIA 1600, 131, and 304 Å images and the *IRIS*/SJ 1400 Å images at 17:30 UT before the flare maximum. As with the other X-class flares, this event displays double ribbons at 1600 Å. One is short near the sunspot, while the other one is long and shows a curved shape. The light curves integrated in the blue box are given in the third panel of Figure 1 at all nine AIA wavelengths. AIA has a pixel size of 0.″6 and a time resolution of 24 s at 1600 and 1700 Å, while 12 s at the other seven EUV wavelengths (Lemen et al. 2012). For the 2014 September 10 flare, AIA images at these seven EUV wavelengths are regularly saturated every 24 s. These saturation images are ruled out to do the analysis. The light curves at these seven EUV wavelengths also have the same 24s time resolution as that at 1600 and 1700 Å. The Slit-Jaw Imager (SJI) on board *IRIS* takes the solar images with a field of view (FOV) of 119″ ×119″ and pixel size of 0.″166. The time cadence is 19 s at 1400 and 2796 Å. The right upper panel in Figure 3 gives one SJI image at 1400 Å, and it also includes the long ribbon of the solar flare. The AIA and SJI images have been pre-processed with the standard solar-software routines (Marc & Greg 2013; Mclntosh et al. 2013) to be aligned. The AIA images at 1600 Å are used to co-align with the SJI images at 1400 Å because both of them include the continuum emissions from the temperature minimum, and the continuum emissions are dominant in many of the bright features. The upper middle and right panels in Figure 3 show the results of the co-alignment between AIA 1600 Å and SJI 1400 Å images at 17:30 UT. They have the same scales and similar bright features. The black line indicates the *IRIS* slit position. The red box in the left panels marks the FOV of the SJI image in the active region. Figure 3 also shows the same regions at AIA 131 Å and AIA 304 Å, which correspond to the high and low temperatures, respectively. We make the movie for Figure 3 from 17:12 UT to 17:58 UT, which contains the impulsive phase of the X1.6 flare (seen in the movie of f3.mpg).

The *IRIS* spectrograph observes AR 12158 from 11:28 UT to 17:58 UT on 2014 September 10 in a "sit-and-stare" mode, and the step cadence is ~9.4 s. The pixel size along the slit is ~0.″166, and the spectral scale is ~12.8 mÅ pixel^{-1} at far-ultraviolet (FUV; FUV1 and FUV2) bands (De Pontieu & Lemen 2013; Mclntosh et al. 2013; De Pontieu et al. 2014). But to save telemetry, two times spectral binning and a restricted number of spectral windows were obtained, i.e., the spectral scale is 25.6 mÅ pixel^{-1}, equivalent to 5.6 km s^{-1} pixel^{-1}. In this case, we used the "flare" list of lines, which consisted of the "1343, Fe XII, O I, Si IV" windows. Figure 4 shows the *IRIS* spectra of FUV1 (e.g., 1343, Fe XII 1349, and O I 1356) and FUV2 (e.g., Si IV 1403) windows at 17:30 UT. They have been processed to remove the

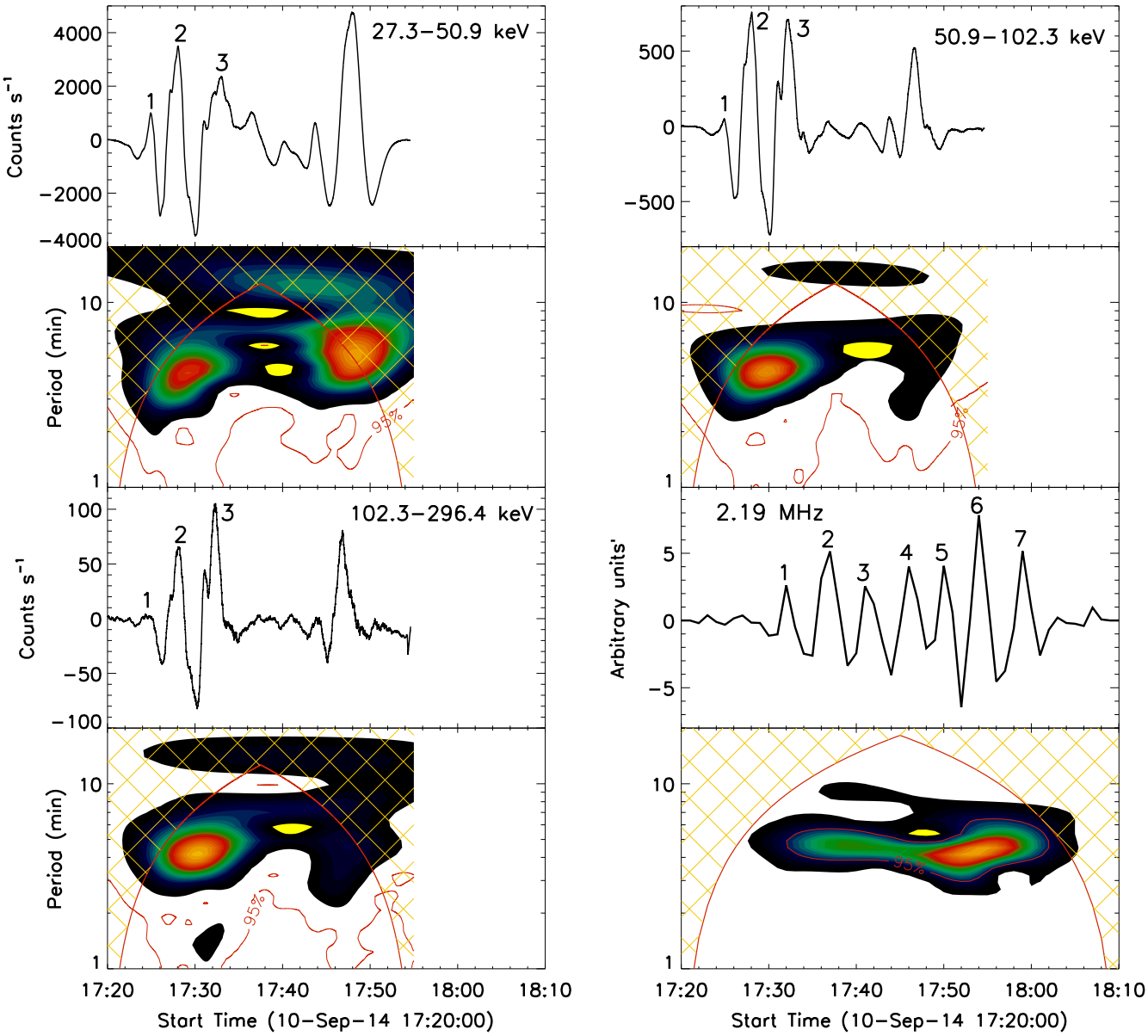

Figure 2. Top: rapidly varying components at *Fermi* 27.3–50.9 keV, 50.9–102.3 keV, 102.3–296.4 keV, and radio emission at frequency of ~2.19 MHz. Bottom: their wavelet power spectra.

bad pixels. Four lines at Fe XXI λ1354.09, C I λ1354.33, O IV λ1399.77, and Si IV λ1402.77 are selected to do analysis. The former two lines are in the FUV1 window, while the O IV and Si IV lines are in the FUV2. It is well known that the forbidden line of Fe XXI λ1354.09 is a broad line and is always blended with other narrow lines from chromospheric emissions, especially the chromospheric line of C I λ1354.33 (e.g., Doschek et al. 1975; Cheng et al. 1979; Mason et al. 1986; Innes et al. 2003a, 2003b), which makes it difficult to fit. *IRIS* has a high spectral resolution of ~26 mÅ, which results in distinguishing a lot of bright emission lines. The upper panel of Figure 4 shows that some of them are well identified, such as C I λ1354.33 (purple line), Fe II λλ1353.07 and 1354.06, and Si II 1353.78, but some of them are still not identified, i.e., λλ1352.77, 1353.40, and 1353.61. These known and unknown bright emission lines that blend with the Fe XXI line must be extracted before determining the Fe XXI intensity. In this case, the fit method described by Li et al. (2015) is used to extract the Fe XXI line information. Briefly, we fixed these bright emission line positions, constrained their widths, and tied their intensities to the lines in other spectral windows. Finally, 15 Gaussian lines superimposed on a linear background are fitted across the whole wavelength region. Only 11 lines are marked with the turquoise vertical ticks in the upper panel of Figure 4. Thus, we can detect the integral intensities, line widths, and Doppler velocities of these lines simultaneously in each fitting, including the chromospheric line of C I λ1354.33 and the coronal line of Fe XXI λ1354.09. The bottom panel of Figure 4 shows the FUV2 windows with four lines, such as O IV λλ1399.77 and 1401.16, S I λ1401.51, and Si IV λ1402.77. Two lines (O IV λ1401.16 and S I λ1401.51) are ruled out to analyze because they are blended with each other, especially during the flare time. The other two lines are isolated and can be well fitted with a single Gaussian function (red lines) to detect the integral intensities, line widths, and Doppler velocities.

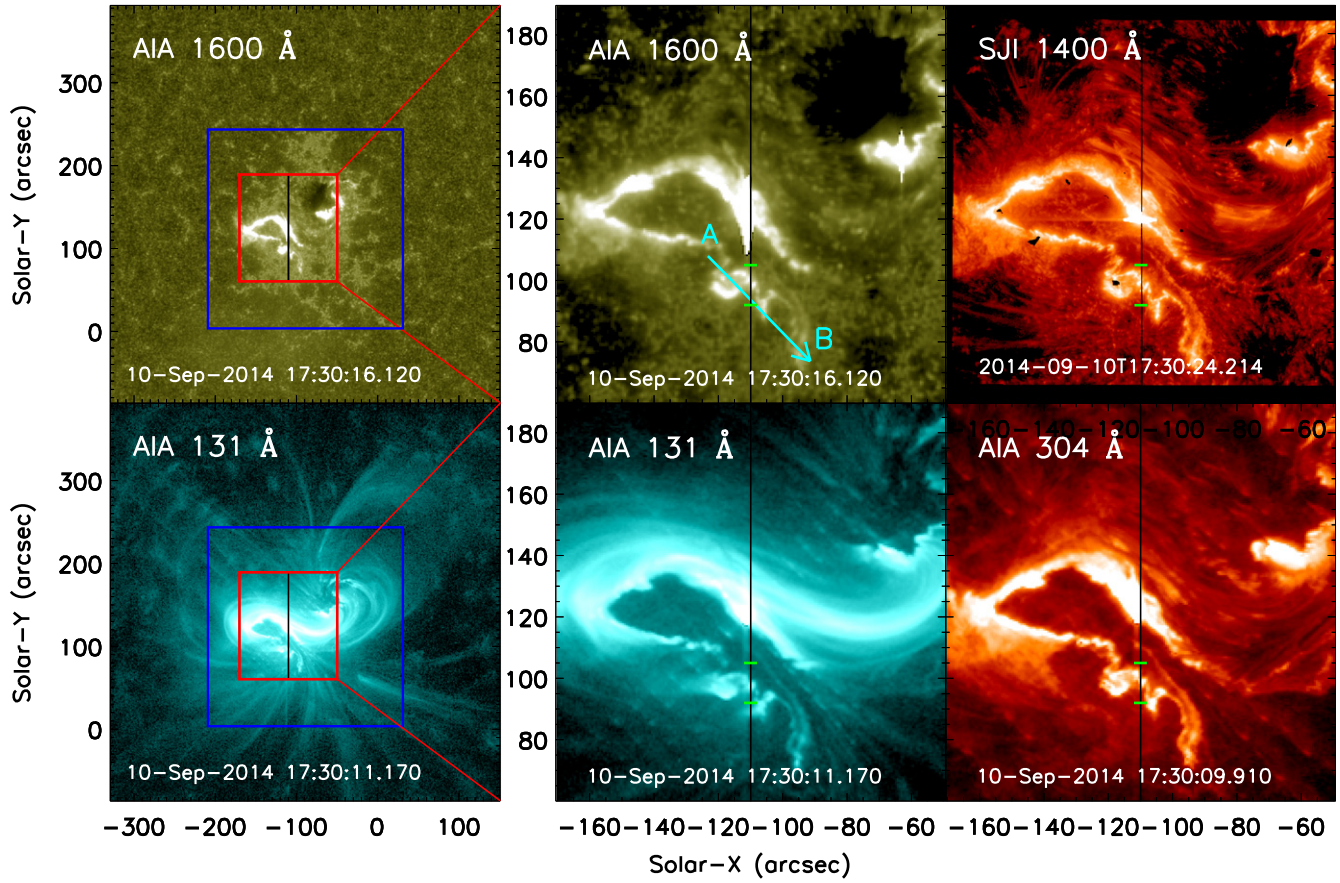

Figure 3. *SDO*/AIA and *IRIS*/SJI images at 17:30 UT on 2014 September 10. Left: AIA images at 1600 and 131 Å. The blue box marks the flare region to integrate the light curves in Figure 1, and the red box gives the FOV of the SJI image. The vertical black lines mark the *IRIS* slit positions. Right: AIA images at 1600, 131, and 304 Å with the same FOV as the SJI image at 1400 Å. Two green solid lines mark a distance of about 10″ along the slit (see details in the text). Arrow "A → B" marks the slit of the spacetime diagram in Figure 9.

(An animation of this figure is available.)

3. RESULTS

Figure 5 shows the spacetime diagrams of the line intensity, line width, and Doppler velocity after fitting four lines C I λ1354.33, Fe XXI λ1354.09, O IV λ1399.77, and Si IV λ1402.77 from 17:12 to 17:58 UT. The *Y*-axis is along the slit, which is fixed on the solar disk. This fact results in the *IRIS* slit observing the same region of the flare ribbon during this interval, as seen in the movie (f3.mpeg). There are two strong emission patterns on these spacetime diagrams. The northern one is wide, and the southern pattern is narrow. This is because the slit straddles the curved flare ribbon, as shown in Figure 3. These two emission patterns are just the different parts of this ribbon. Different from the wide (northern) pattern, the narrow one displays the intensity variation with the time, including the C I, Fe XXI, O IV, and Si IV lines. This behavior is similar to that of the QPPs shown in the HXR and radio emissions. In order to analyze this feature in detail, we first use two lines to trace the southern narrow emission pattern, as shown in Figure 5. The distance between these two lines is a constant of about 10″, as the distance along the slit between two short green lines in Figure 3. Second, the intensities between these two lines are integrated. Thus, we get the intensity light curves of C I, Fe XXI, O IV, and Si IV lines. Figure 6 shows that there are 10 peaks on their intensity light curves from 17:24 UT to 17:56 UT, roughly with a quasi-period of less than 4 minutes. It is clear that these peaks are superposed on a gradual component. Using the same method as shown in Figure 2, Figure 6 (upper left panel) shows that the C I light curve is decomposed into a slowly varying and a rapidly varying component. The slowly varying component is smoothing a window of 28 points. The rapidly varying component is the C I light curve subtracting the slowly varying component. These 10 peaks are clearly shown as marked by the numbers, and they are identified as the QPPs. The wavelet spectra confirm the quasi-period of less than 4 minutes. Such QPPs are also distinctly detected from the O IV and Si IV light curves. There are some signatures of the QPPs on Fe XXI light curves, especially the first three peaks. The other seven peaks of the Fe XXI line are weak. Figure 6 gives the temporal evolution of the Doppler velocities and line widths at C I, Fe XXI, O IV, and Si IV lines. The flare ribbon displays the redshifts on the Doppler velocities of these four lines. The mean velocities between 17:24 UT and 17:58 UT are 67.4, 121.4, 297.9, and 535.7 km s^{-1} at C I, Fe XXI, O IV, and Si IV lines, respectively, as listed in Table 1. There are also some peaks on the Doppler velocities corresponding to that on the intensities, but not one-by-one. The flare ribbon exhibits a broad line width, and the mean values between 17:24 UT and 17:58 UT are 73.9, 514.1, 291.2, and 247.3 pixels at C I, Fe XXI, O IV, and Si IV lines, respectively (see Table 1). There are some peaks on the line widths corresponding to the QPP peaks too.

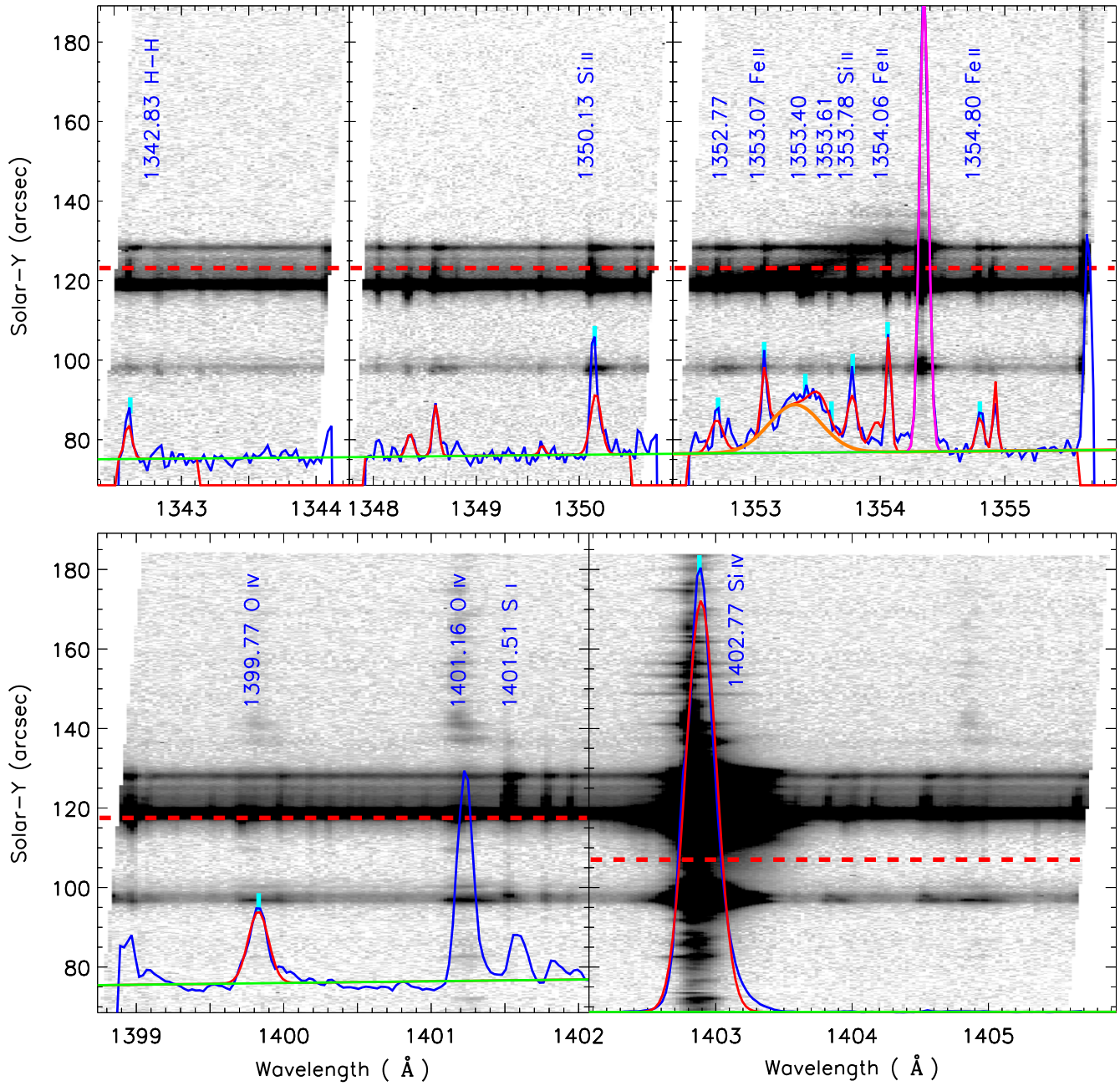

Figure 4. *IRIS* spectra at 17:30 UT from FUV1 (upper; e.g., 1343, Fe XII λ1349, and O I λ1356) and FUV2 (bottom) bands (e.g., Si IV λ1403). The blue spectral profiles are from the flare ribbon at the slit positions marked by the red dashed lines. The horizontal green lines mark the background profiles. The orange profile is the Fe XXI fitting, and the purple profile is the C I fitting. The main lines used to fit for this flare are labeled and indicated by the turquoise vertical ticks just above the line spectra.

Using the same method, their Doppler velocities and line widths are decomposed into the slowly varying and rapidly varying components. The wavelet spectra of the rapidly varying components of Doppler velocity and line width also exhibit the similar 4-minute QPP features.

The *SDO*/AIA movie shows that the flare ribbon evolves from the northeast toward the southwest on the solar disk, which results in the flare ribbon crossing the *IRIS* slits. The onset time at 17:24 UT in Figure 6 is not the flare beginning time but represents the starting time of the flare ribbon entrance into the slit window. It is hard to detect the QPP starting time from the flare ribbon. However, an artificial slit with a position the same as the *IRIS* slit is put on the AIA images. Thus, we get the spacetime diagrams from AIA observations, as shown in Figure 7. As with the *IRIS* observation in Figure 5, there are two bright patterns corresponding to the two parts of the flare ribbon. There are intensity flashes at the southern small region. Using the same two lines in Figure 5, the light curves between them are shown in Figure 8 at nine AIA wavelengths. The QPPs are clearly seen on their light curves. Ten individual peaks are recognized between 17:24 UT and 17:56 UT, which is the same as in the *IRIS* observations, and each peak of QPPs is marked with numbers. The light curves are also decomposed into the slowly varying (blue dashed line) and rapidly varying components, whose wavelet spectra are also shown. The QPPs exhibit a period of less than 4 minutes again, which is similar to

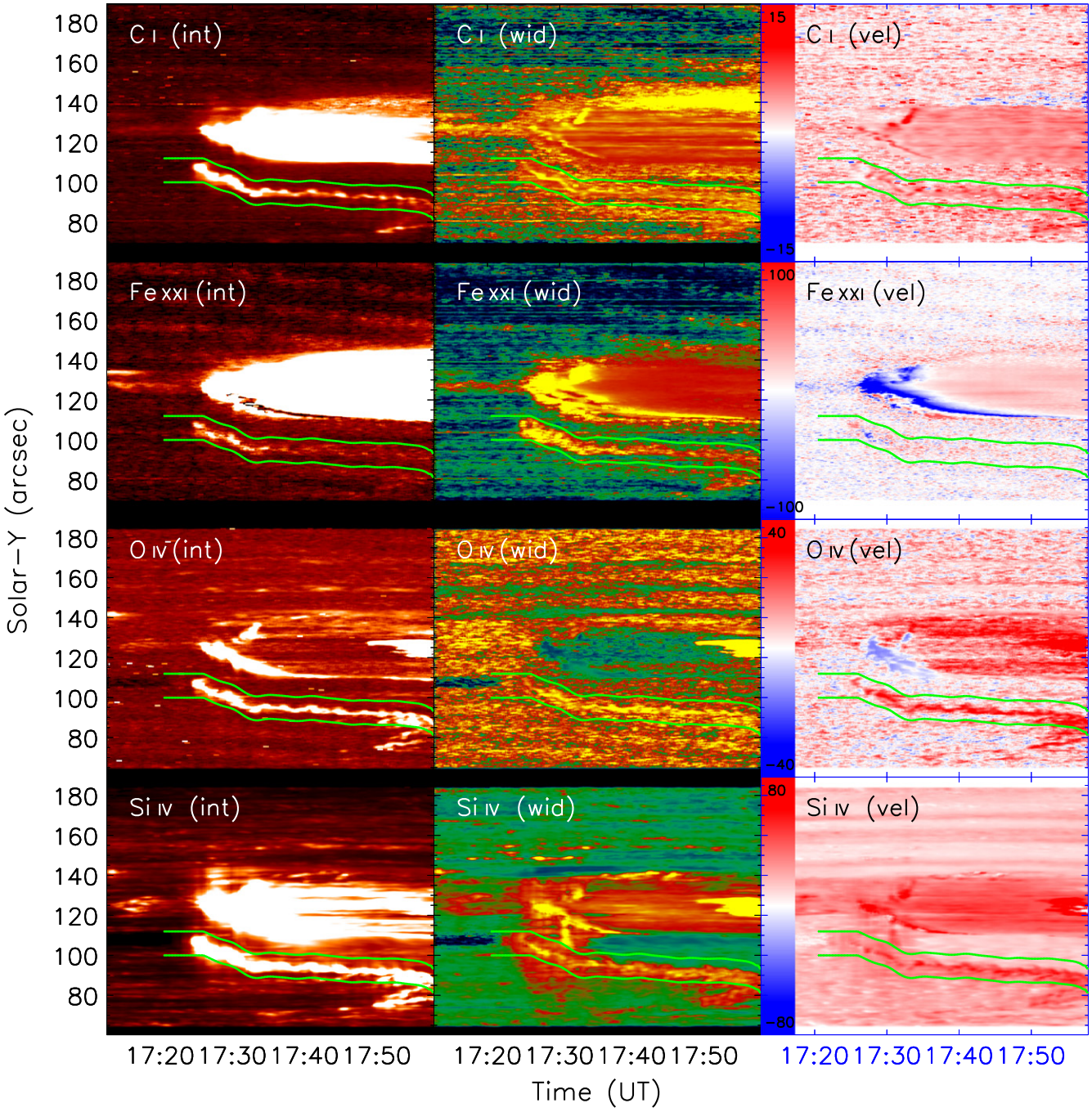

Figure 5. Spacetime diagrams of line intensity (left), line width (middle), and Doppler velocity (right) from *IRIS* observations, such as C I, Fe XXI, O IV, and Si IV lines. The light curves integrated between two green lines are shown in Figure 6.

that in the spectral lines at C I, Fe XXI, O IV, and Si IV from *IRIS* observations.

4. CONCLUSIONS AND DISCUSSIONS

Based on the multiwavelength observations from *Fermi*/GBM, *SDO*/AIA, *IRIS*, and SWAVES, we analyze the imaging and spectral observations of the 4-minute QPPs at HXR, EUV, and radio emissions in a solar flare on 2014 September 10. We draw the following conclusions.

(I) The 4-minute QPPs are found in a broad frequency range from HXR through EUV to the radio.

(II) Imaging observations of *SDO*/AIA show that the QPPs originate from the flare ribbon front.

(III) Spectral observations of *IRIS* present that the QPP peaks tend to a broad line width and a redshift velocity.

Although there are several models to explain the QPPs in the documents (e.g., Aschwanden 1987; Nakariakov et al. 2004; Nakariakov & Melnikov 2009), our findings support that the QPPs are produced by the non-thermal electron beams accelerated by the periodic magnetic reconnection in this flare. In this case, each individual peak of the QPPs is radiated by the different electron beams. Based on the standard flare model, each magnetic reconnection can accelerate the bi-directional

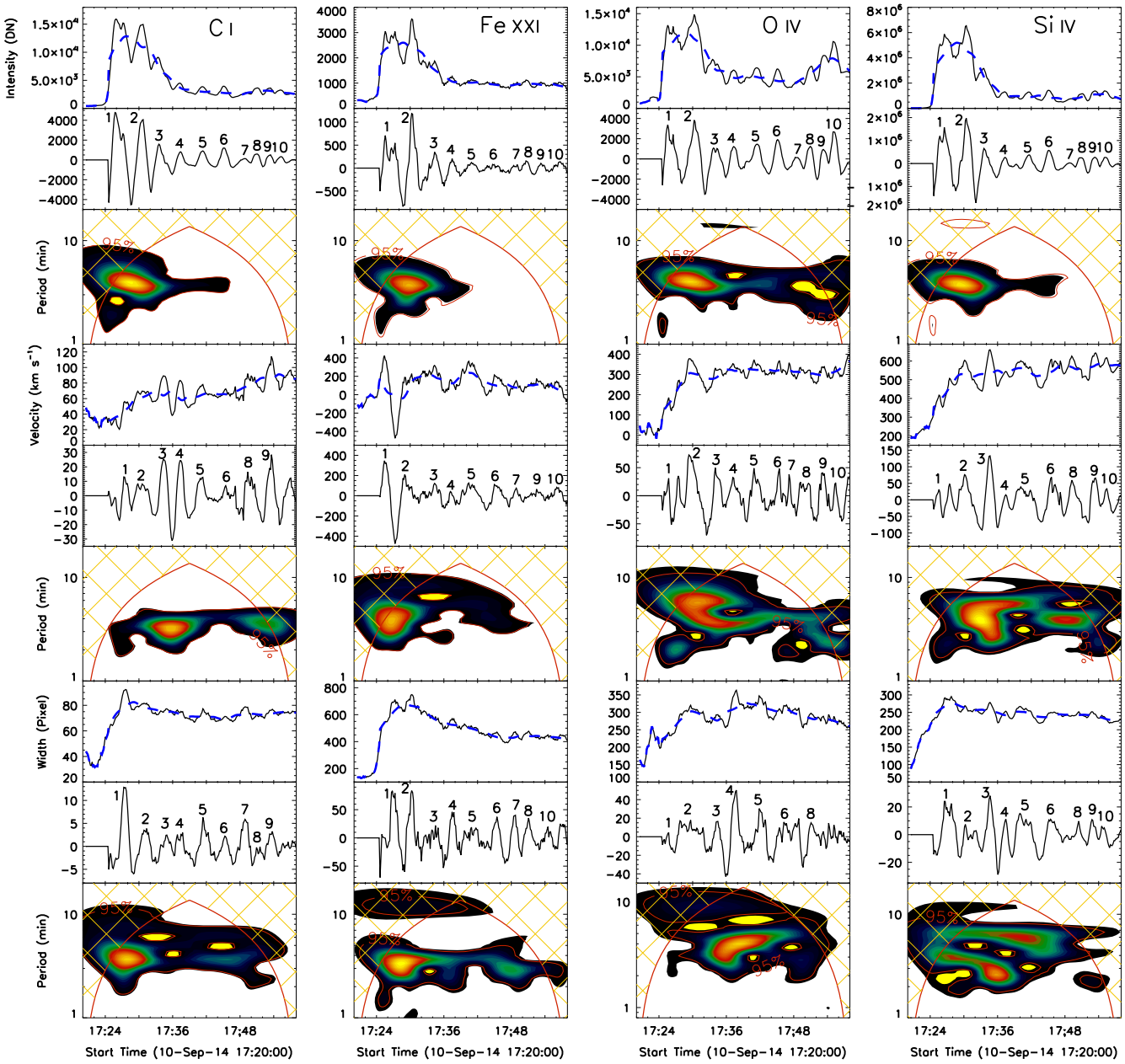

Figure 6. Time evolution of intensity (row 1), Doppler velocity (row 4), and line width (row 7) at the lines of C I (column 1), Fe XXI (column 2), O IV (column 3), and Si IV(column 4). The blue dashed lines represent the slowly varying components. Rows 2, 5, 8: their rapidly varying components. Rows 3, 6, 9: their wavelet power spectra.

Table 1
Mean Value and Standard Deviation of Doppler Velocities and Line Widths between 17:24 UT and 17:58 UT of the Spectral Lines from *IRIS* Observations

Spectrum	Doppler Velocity (km s^{-1})		Line Width (pixels)	
	Mean	Standard Deviation	Mean	Standard Deviation
C I	67.4	17.9	73.9	5.1
Fe XXI	121.4	140.4	514.1	91.2
O IV	297.9	55.7	291.2	27.8
Si IV	535.7	65.9	247.3	16.8

electron beams simultaneously (e.g., Heyvaerts et al. 1977; Aschwanden et al. 1995; Innes et al. 1997; Ning et al. 2000; Ji et al. 2006, 2008; Shen et al. 2008; Feng et al. 2011; Zhang et al. 2012, 2014; Feng & Wang 2013; Su et al. 2013). The upward beam radiates the type III bursts on its trajectory propagation into the outer corona. The downward beam produces one peak at HXR when it injects into the chromosphere to heat the local plasma, on its way producing one peak at EUV. In this case, the periodic magnetic reconnection can produce the QPP peaks at HXR and radio type III bursts, and the periodic EUV emissions as well. In other words, the periodic magnetic reconnection model can well explain the QPPs from HXR through EUV to the radio emissions in the 2014 September 10 solar flare. In general, the other models also explain the QPP features, especially at HXR and EUV bands (e.g., Ofman & Wang 2002; Foullon et al. 2005; Su et al. 2012a), i.e., the MHD flux tube oscillations, modulated by certain waves or periodic self-organizing systems of plasma instabilities. As mentioned earlier, solar type III bursts are

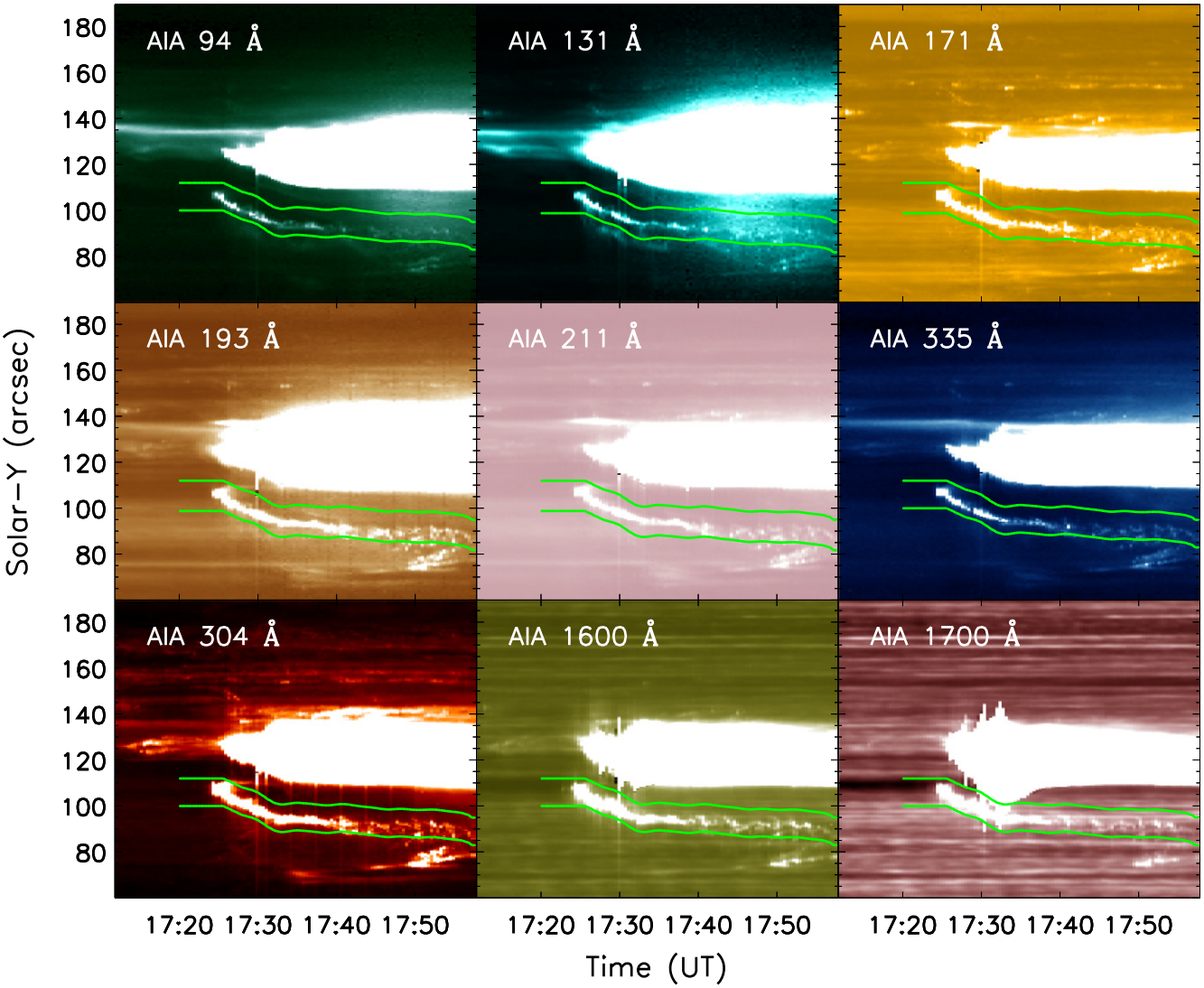

Figure 7. Same as Figure 5, but the spacetime diagrams at nine AIA wavelengths from the same position as the *IRIS* slit.

produced by the electron beams propagating into the outer corona and then into the interplanetary. In other words, a group of type III bursts are produced by various electron beams. Therefore, the periodic solar type III bursts provide direct evidence of the periodic magnetic reconnection in this flare.

It is still an open question what determines the period. The quasi-periodic magnetic reconnection may be spontaneous (Kliem et al. 2000; Karlický 2004; Karlický et al. 2005; Murray et al. 2009), or could be modulated by certain waves in the solar corona (Aschwanden et al. 1994a; Aschwanden 2004; Chen & Priest 2006; Nakariakov et al. 2006; Ofman & Sui 2006; Inglis & Nakariakov 2009; Liu et al. 2011; Nakariakov & Zimovets 2011; Li & Zhang 2015). In the case of spontaneous quasi-periodicity, it is not understood yet what determines the period (e.g., Kliem et al. 2000; Murray et al. 2009). In the latter induced case, the periodic triggering of the reconnection can be some MHD oscillations, as were shown in several papers (e.g., Chen & Priest 2006; Nakariakov et al. 2006; Nakariakov & Zimovets 2011). The period of the observational QPPs is thought to be associated with one of the MHD modes. There are three possibilities for such MHD wave modes that may trigger the periodic magnetic reconnection in our case. The first possibility is the quasi-periodic reconnection modulated by slow waves (Chen & Priest 2006). For example, the 3- or 5-minute solar *p*-mode oscillations (slow waves) can trigger the quasi-periodic magnetic reconnection with a similar period when the reconnection site is located in the upper chromosphere (Ning et al. 2004). This is similar to the 4-minute period of QPPs in the 2014 September 10 flare. However, this model depends strongly on the location of the reconnection site in the solar atmosphere, and it becomes weaker when the reconnection site is lower or higher than the upper chromosphere. The second possibility is the quasi-periodic reconnection modulated by fast waves. Nakariakov et al. (2006) suggest that the fast waves in a corona loop situated near the flare site can trigger the quasi-periodic magnetic reconnection. In particular, the global kink mode (Foullon et al. 2005) can trigger the quasi-periodic magnetic reconnection and produce the QPPs with a period of about several minutes. This model is used to explain the min-periodic phenomena in solar flares. The third case is the slow magnetoacoustic waves to modulate the quasi-periodic reconnection. Nakariakov & Zimovets (2011) have demonstrated that the slow magnetoacoustic waves can propagate along the

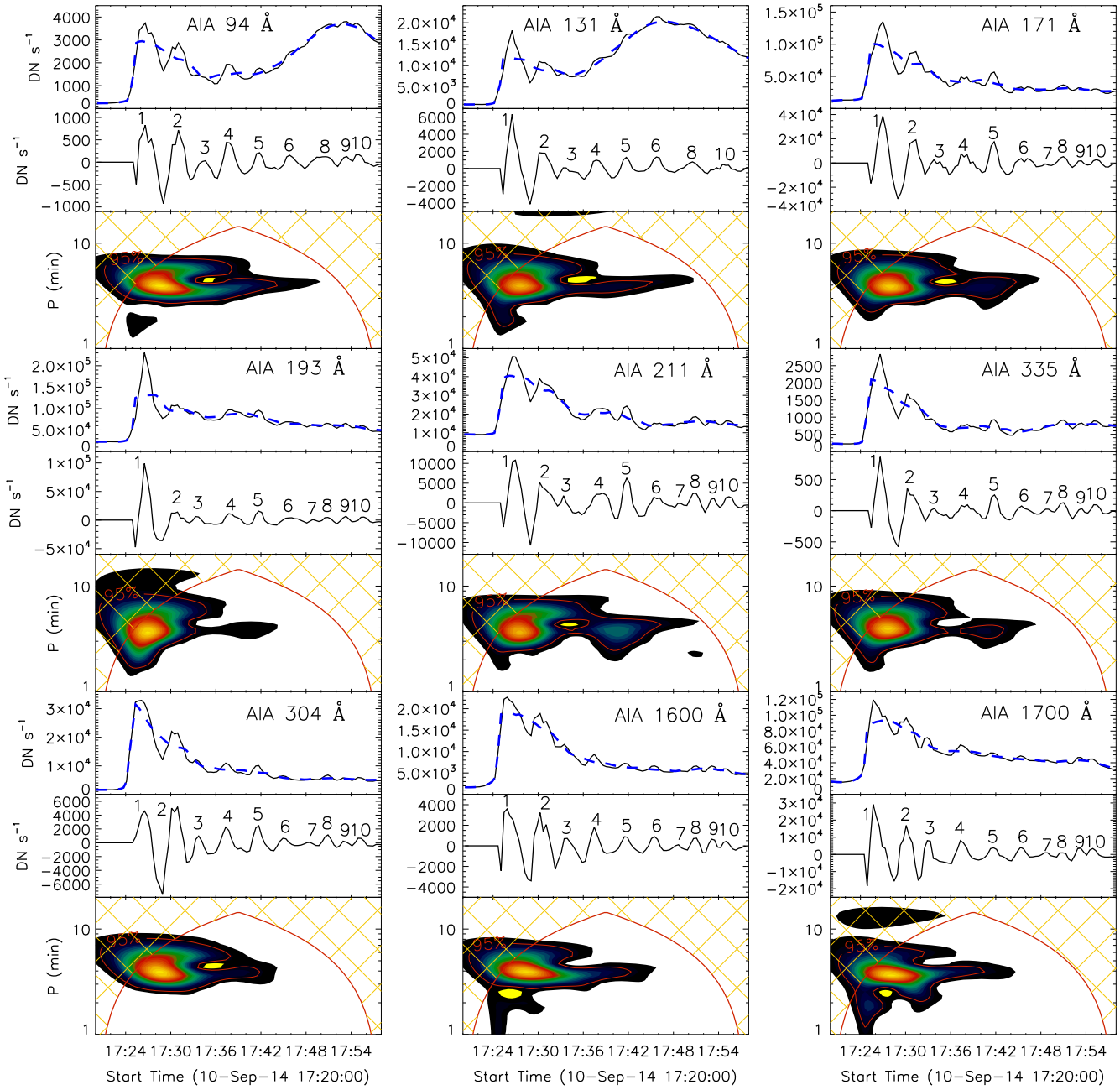

Figure 8. Rows 1, 4, 7: the light curves integrate between two green lines in Figure 7 at all AIA nine wavelengths. The blue dashed lines are the slowly varying components. Rows 2, 5, 8: their rapidly varying components. Rows 3, 6, 9: their wavelet power spectra.

axis of a coronal magnetic arcade, then possibly triggering the quasi-periodic reconnection during the solar flare. The observational period is similar to the period of a standing slow magnetoacoustic wave in the loops that form the arcade. They suggest that the QPPs observed in two-ribbon flares can be explained with this mechanism. Namely, such a mechanism can explain the 4-minute period of QPPs in the 2014 September 10 flare. This is because we find that the brightness structures move along the flare ribbon parallel to the magnetic neutral line (seen in the movie of f3.mpeg). Figure 9 (upper panel) shows the spacetime slices along the flare ribbon A → B on the AIA 1600 Å image in Figure 3. There are many brightening structures moving from A to B. The propagation speed is roughly estimated to be 15–40 km s^{-1}, which is consistent with previous findings (e.g., Bogachev et al. 2005; Krucker et al. 2005; Tripathi et al. 2006; Li & Zhang 2009, 2015; Reznikova et al. 2010; Nakariakov & Zimovets 2011). These values are much smaller than the local Alfvén and sound speeds. The moving brightening structures are thought to be the evidences of the slow magnetoacoustic waves across the magnetic fields in solar flares (Nakariakov & Zimovets 2011).

The delay of about 8 minutes between the HXR (or EUV) and radio emissions in this flare is possibly due to the different sites of the radio sources (electron beams for type III bursts) from HXR or EUV sources. Usually, HXR and EUV emissions are produced at the chromosphere or lower corona, while the radio source around 2 MHz originates from a heliocentric height of about 10 $R_\odot$ (Krupar et al. 2014). The time of the electron beams (type III bursts source) propagating from the flare site (acceleration region) to ∼10 $R_\odot$ roughly equals the

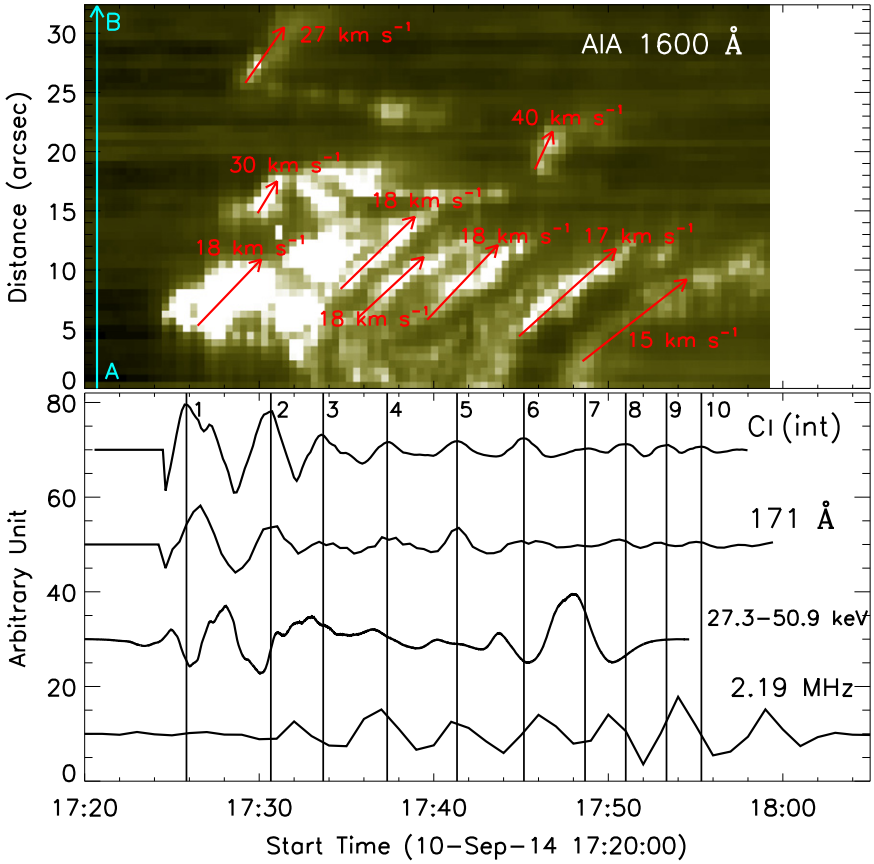

Figure 9. Upper: AIA 1600 Å spacetime diagram along the slit "A → B" in Figure 3. Bottom: illustration of the QPPs at *IRIS* C I line, AIA 171 Å, *Fermi* 27.3–50.9 keV, and SWAVES 2.19 MHz.

delay between HXR (or EUV) and radio emissions. Based on this assumption, we estimate that the electron beams (radio sources) have a speed of ~0.05*c* (*c* is the light speed in a vacuum). This value is reasonable for the electron beams propagating outward from the Sun in the interplanetary medium (e.g., Dulk et al. 1987; Krupar et al. 2014). Figure 9 (bottom) plots the QPPs at *IRIS* C I intensity, AIA 171 Å, *Fermi* 27.3–50.3 keV, and SWAVES 2.19 MHz. Each peak of the QPPs at C I intensity well corresponds to that at AIA 171 Å. However, they are not correlated to the HXR and radio peaks, which could result from the radiation source positions.

The authors would like to thank the anonymous referee for valuable comments to improve the manuscript. The data used in this paper are from *Fermi*, *STEREO*, *SDO*/AIA, *IRIS*, and *GOES*. This study is supported by NSFC under grants 11073058, 11073006, 11173062, 11203083, 11333009, 11303101, 11473071, 973 program (2011CB811400, 2014CB744200), and Laboratory No. 2010DP173032. We are grateful to D. E. Innes for *IRIS* data, I. Sharykin, A. Struminsky, and W. Chen for *Fermi* data, Y. Huang for *STEREO* data, and L. Xu for helpful discussions.

REFERENCES

Asai, A., Shimojo, M., Isobe, H., et al. 2001, ApJL, 562, L103
Aschwanden, M. J. 1987, SoPh, 111, 113
Aschwanden, M. J. 2004, ApJ, 608, 554
Aschwanden, M. J., Benz, A. O., Dennis, B. R., & Kundu, M. R. 1994a, ApJS, 90, 631
Aschwanden, M. J., Benz, A. O., Dennis, B. R., & Schwartz, R. A. 1995, ApJ, 455, 347
Aschwanden, M. J., Benz, A. O., & Montello, M. L. 1994b, ApJ, 431, 432
Aschwanden, M. J., De Pontieu, B., Schrijver, C. J., & Title, A. M. 2002, SoPh, 206, 99
Aschwanden, M. J., Kliem, B., Schwarz, U., et al. 1998, ApJ, 505, 941
Bogachev, S. A., Somov, B. V., Kosugi, T., & Sakao, T. 2005, ApJ, 630, 561
Bogovalov, S. V., Iyudin, A. F., Kotov, Y. D., et al. 1983, SvAL, 9, 163
Bogovalov, S. V., Iyudin, A. F., Kotov, Y. D., et al. 1984, SvAL, 10, 286
Chen, P. F., & Priest, E. R. 2006, SoPh, 238, 313
Cheng, C.-C., Feldman, U., & Doschek, G. A. 1979, ApJ, 233, 736
De Moortel, I., Ireland, J., Hood, A. W., & Walsh, R. W. 2002, A&A, 387, L13
De Pontieu, B., & Lemen, J. 2013, IRIS Technical Note 1—IRIS Operations, version 17: 22
De Pontieu, B., Title, A. M., Lemen, J. R., et al. 2014, SoPh, 289, 2733
Doschek, G. A., Dere, K. P., Sandlin, G. D., et al. 1975, ApJL, 196, L83
Dulk, G. A., Goldman, M. V., Steinberg, J. L., & Hoang, S. 1987, A&A, 173, 366
Feng, H., & Wang, J. 2013, A&A, 559, A92
Feng, H. Q., Wu, D. J., Wang, J. M., & Chao, J. W. 2011, A&A, 527, A67
Foullon, C., Verwichte, E., Nakariakov, V. M., & Fletcher, L. 2005, A&A, 440, L59
Heyvaerts, J., Priest, E. R., & Rust, D. M. 1977, ApJ, 216, 123
Hoyng, P., van Beek, H. F., & Brown, J. C. 1976, SoPh, 48, 197
Inglis, A. R., & Nakariakov, V. M. 2009, A&A, 493, 259
Innes, D. E., Inhester, B., Axford, W. I., & Wilhelm, K. 1997, Natur, 386, 811
Innes, D. E., McKenzie, D. E., & Wang, T. 2003a, SoPh, 217, 247
Innes, D. E., McKenzie, D. E., & Wang, T. 2003b, SoPh, 217, 267
Ji, H., Huang, G., Wang, H., et al. 2006, ApJL, 636, L173
Ji, H., Wang, H., Liu, C., & Dennis, B. R. 2008, ApJ, 680, 734
Karlický, M. 2004, A&A, 417, 325
Karlický, M., Bárta, M., Mészárosová, H., & Zlobec, P. 2005, A&A, 432, 705
Kliem, B., Dammasch, I. E., Curdt, W., & Wilhelm, K. 2002, ApJL, 568, L61
Kliem, B., Karlický, M., & Benz, A. O. 2000, A&A, 360, 715
Krucker, S., Fivian, M. D., & Lin, R. P. 2005, AdSpR, 35, 1707
Krupar, V., Maksimovic, M., Santolik, O., et al. 2014, SoPh, 289, 3121

Kupriyanova, E. G., Melnikov, V. F., Nakariakov, V. M., & Shibasaki, K. 2010, SoPh, 267, 329
Lemen, J. R., Title, A. M., Akin, D. J., et al. 2012, SoPh, 275, 17
Li, D., Innes, D. E., & Ning, Z. J. 2015, A&A, submitted
Li, L., & Zhang, J. 2009, ApJ, 690, 347
Li, T., & Zhang, J. 2015, ApJL, 804, L8
Li, Y. P., & Gan, W. Q. 2008, SoPh, 247, 77
Lipa, B. 1978, SoPh, 57, 191
Liu, W., Title, A. M., Zhao, J., et al. 2011, ApJL, 736, L13
Mangeney, A., & Pick, M. 1989, A&A, 224, 242
Marc, D., & Greg, S. 2013, Guide to SDO Data Analysis (edited on 2013 February 19)
Mariska, J. T. 2005, ApJL, 620, L67
Mariska, J. T. 2006, ApJ, 639, 484
Mason, H. E., Shine, R. A., Gurman, J. B., & Harrison, R. A. 1986, ApJ, 309, 435
Mclntosh, S. W., De Pontieu, B., Hansteen, V., & Boerner, P. 2013, A Users Guide To IRIS Data Retrieval, Reduction and Analysis, 2013 October 30
Meegan, C., Lichti, G., Bhat, P. N., et al. 2009, ApJ, 702, 791
Murray, M. J., van Driel-Gesztelyi, L., & Baker, D. 2009, A&A, 494, 329
Nakajima, H., Kosugi, T., Kai, K., & Enome, S. 1983, Natur, 305, 292
Nakariakov, V. M., Foullon, C., Myagkova, I. N., & Inglis, A. R. 2010, ApJL, 708, L47
Nakariakov, V. M., Foullon, C., Verwichte, E., & Young, N. P. 2006, A&A, 452, 343
Nakariakov, V. M., & Melnikov, V. F. 2009, SSRv, 149, 119
Nakariakov, V. M., Ofman, L., Deluca, E. E., Roberts, B., & Davila, J. M. 1999, Sci, 285, 862
Nakariakov, V. M., Tsiklauri, D., Kelly, A., Arber, T. D., & Aschwanden, M. J. 2004, A&A, 414, L25
Nakariakov, V. M., & Zimovets, I. V. 2011, ApJL, 730, L27
Ning, Z. 2014, SoPh, 289, 1239
Ning, Z., Ding, M. D., Wu, H. A., Xu, F. Y., & Meng, X. 2005, A&A, 437, 691
Ning, Z., Fu, Q., & Lu, Q. 2000, A&A, 364, 853
Ning, Z., Innes, D. E., & Solanki, S. K. 2004, A&A, 419, 1141
Ofman, L., & Sui, L. 2006, ApJL, 644, L149
Ofman, L., & Wang, T. 2002, ApJL, 580, L85
Reznikova, V. E., Melnikov, V. F., Ji, H., & Shibasaki, K. 2010, ApJ, 724, 171
Roberts, B., Edwin, P. M., & Benz, A. O. 1984, ApJ, 279, 857
Rucker, H. O., Macher, W., Fischer, G., et al. 2005, AdSpR, 36, 1530
Shen, J., Zhou, T., Ji, H., et al. 2008, ApJL, 686, L37
Su, J. T., Shen, Y. D., & Liu, Y. 2012a, ApJ, 754, 43
Su, J. T., Shen, Y. D., Liu, Y., Liu, Y., & Mao, X. J. 2012b, ApJ, 755, 113
Su, Y., Veronig, A. M., Holman, G. D., et al. 2013, NatPh, 9, 489
Sych, R., Nakariakov, V. M., Karlicky, M., & Anfinogentov, S. 2009, A&A, 505, 791
Tan, B., Zhang, Y., Tan, C., & Liu, Y. 2010, ApJ, 723, 25
Tian, H., McIntosh, S. W., & De Pontieu, B. 2011, ApJL, 727, L37
Tripathi, D., Isobe, H., & Mason, H. E. 2006, A&A, 453, 1111
Wang, T. J., Solanki, S. K., Curdt, W., Innes, D. E., & Dammasch, I. E. 2002, ApJL, 574, L101
Wang, T. J., Solanki, S. K., Curdt, W., et al. 2003, A&A, 406, 1105
Zhang, Q. M., Chen, P. F., Ding, M. D., & Ji, H. S. 2014, A&A, 568, A30
Zhang, Q. M., Chen, P. F., Guo, Y., Fang, C., & Ding, M. D. 2012, ApJ, 746, 19
Zhao, R. Y., Mangeney, A., & Pick, M. 1991, A&A, 241, 183
Zimovets, I. V., & Struminsky, A. B. 2010, SoPh, 263, 163